Ga–Mg Core–Shell Nanosystem for a Novel Full Color Plasmonics

ARTICLE *in* THE JOURNAL OF PHYSICAL CHEMISTRY C · JULY 2011

Impact Factor: 4.77 · DOI: 10.1021/jp201423r

THE JOURNAL OF PHYSICAL CHEMISTRY C

ARTICLE

pubs.acs.org/JPCC

Ga−Mg Core−Shell Nanosystem for a Novel Full Color Plasmonics

Pae C Wu,[†] Maria Losurdo,[*,†,‡] Tong-Ho Kim,[†] Borja Garcia-Cueto,[§] Fernando Moreno,[§] Giovanni Bruno,[‡] and April S. Brown[†]

[†]Department of Electrical and Computer Engineering, Duke University, Durham, North Carolina 27708, United States

[‡]IMIP-CNR, University of Bari, via Orabona 4, 70126 Bari, Italy

[§]Departamento Física Aplicada, Grupo de Óptica, Universidad de Cantabria, 39005 Santander, Spain

ABSTRACT: Gallium−magnesium (Ga−Mg) core−shell nanoparticles were synthesized by sequential evaporation of gallium and magnesium molecular beams on sapphire substrates. The surface plasmon resonance properties of this novel bimetallic system are demonstrated and investigated in a broad spectral range, from the near-UV to the visible and to the near-IR by in situ real-time spectroscopic ellipsometry. Both the mean NP ensemble diameter and the relative core−shell radii affect the resultant plasmon resonance, and this study shows that the resonance can be red-shifted and tuned into the near-IR by increasing the extent of the Mg-shell, while limiting the overall nanoparticle size, promoting this novel, nanomaterials system for applications of bifunctional plasmonic-catalytic nanoparticles with optical properties tunable across a broad spectral range. Experimental real-time plasmonic results are corroborated by discrete dipole approximation calculations applied to core−shell nanoparticles supported on the substrate, which rationalize the red-shift of the Ga−Mg core−shell structure with the increase of the Mg shell relative volume.

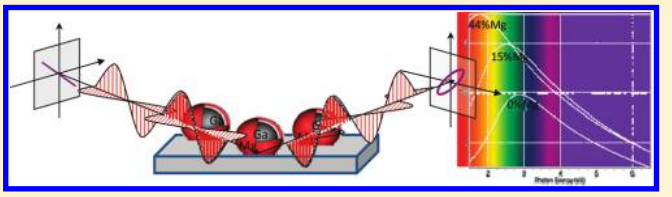

1. INTRODUCTION

Plasmonic nanoparticles (NPs) play an integral role in developing technologies ranging from sensors, imagers, photodiagnostics, biomolecular optical markers, optoelectronics, surface-enhanced Raman spectroscopy substrates, and ultrafast nonlinear optical devices, which drives the significant research efforts toward developing advanced, novel bimetallic nanoparticles.[1−4]

Significant progress has been made in the synthesis of NPs with different shape, geometry, and composition. Alloyed and layered core−shell metal nanostructures are considered for expanding the tunability of their surface plasmon resonance (SPR) as an interesting case where all of the parameters together with size, morphology, geometry, and composition of the shell and the core are exploited simultaneously. One of the most fascinating aspects of core−shell structures is that their optical properties can be varied by using different combinations of shell and core thickness and materials.[5]

With the control demonstrated over the size or shape of noble metal NPs, the achievable range of plasmon resonance tuning of single metal NPs by size and shape modification has been largely extended to the near-infrared (NIR). For example, Au nanospheres of increasing size give resonances between 520 and 580 nm,[6−8] whereas Ag NP plasmons can reach resonances as short as 380 nm,[8−11] though they are hampered by a chemical instability characterized by a quenched plasmon resonance upon air exposure.[9] Modifying the shape, e.g. high aspect ratio nanorods, adds a degree of freedom for the electron density oscillations splitting the plasmon modes such that the longitudinal plasmon modes of gold nanorods can be tuned from the visible to near-infrared up to 1600 nm, depending on their aspect ratio.[12,13]

Nanoshells have attracted interest because they have been shown to exhibit a much higher sensitivity than solid colloids in response to the changes occurring on their surfaces,[14] and depending on the thickness of the shell, a red-shift of the SPR to 720 nm for Au nanoshells has also been achieved.[15]

Nevertheless, broad interband transitions featured in the Au bulk dielectric function limit its tunability further to the blue, unlike other plasmonic metals such as Al or Ag.[16−18]

Recently, Ga, which possesses a large bulk plasma frequency of 14.3 eV, has been demonstrated to boast a broadly tunable SPR from the NIR into the UV.[19,20] Despite its broad plasmon range, simply modifying the Ga plasmon resonance by size is untenable in situations that require small particles with long wavelength plasmons such as plasmonic waveguides for optical communications systems, where the subwavelength dimensions of plasmonic waveguides enable the transfer of optical signals along NP chains whose critical dimension falls below the diffraction limit.[21−23]

Alloying combining multiple metals to varying compositions is an alternative to modifying the metal properties without sacrificing nanoparticle size. A detailed theoretical analysis of fiber optic SPR sensors determined that no single metal plasmonic NP system (Ag, Au, Al, or Cu) can simultaneously provide reasonable performance in three critical metrics − sensitivity, SNR (signal-to-noise ratio), and operating range − unlike bimetallic NPs.[24] Previous studies on binary metal core−shell[25−27] or alloyed/mixed metal nanoparticles[27−34] typically focused on noble

Received: February 13, 2011
Revised: June 10, 2011
Published: June 11, 2011

metals, e.g., Ag−Au, Au−Ag nanoshells,[35,36] Ag−Pt, Au−Cu,[37] and Au−Pd.[38,39]

In this work we create a new bimetallic plasmonic system of Ga-core/Mg-shell nanoparticles where the SPR can be tuned in a broad spectral range from the UV to the NIR. Ga and Mg have plasma frequencies of 14.3 and 10.5 eV, respectively, which are larger than Ag and Au, and therefore are expected to produce mixed metal nanoparticles resonant in the UV.[40,41] Ga, which boasts oxidation and thermal stability along with a wide plasmon range,[19,28,42−44] is combined with Mg,[45] which is technologically relevant also for hydrogen storage and catalysis.[46] Ga can dissociate H_2,[47] as such the dissociative chemisorption of H_2 on Ga−Mg mixtures makes this bimetallic mixture potentially viable for alternative energy technology in addition to plasmonics. Moreover, unlike Au and Cu, whose strong interband transitions limit their plasmon resonance ranges, Mg is a free electron metal making it an advantageous alloying component for plasmonic tuning.[45] However, a disadvantage of pure Mg plasmonic NPs is their tendency to oxidize, which redshifts ($\Delta E = 4$ eV) and ultimately quenches their plasmon resonance,[41] a characteristic Ga may mitigate against since the Ga SPR is thermally stable and does not quench when oxidized.[19]

Therefore, here, we synthesize and analyze the Ga-core/Mg-shell bimetallic nanoparticles with varying relative radii, but with fixed NP diameter to demonstrate the SPR's compositional dependence. Spectroscopic ellipsometry is used to monitor and tailor in real time the nanoparticles surface plasmon resonance. Electron energy loss spectroscopy (EELS) has been used to record the surface plasmon peak from single Ga−Mg core−shell nanoparticles and energy-filtered TEM (EFTEM) to visualize the spatial extent of the surface plasmon. The optical response of the Ga-core/Mg-shell bimetallic nanoparticles is also calculated using the discrete dipole approximation (DDA),[48] which is a numerical method used to calculate the electromagnetic interaction with targets of arbitrary shape, therefore, corroborating and rationalizing the experimental observations.

2. EXPERIMENTAL SECTION

Deposition and Characterization of Nanoparticles. Ga−Mg core−shell NPs were deposited by molecular beam epitaxy at 25 °C on sapphire substrates. We sequentially deposit Ga and Mg such that Ga seed NPs are coated with Mg overlayers while keeping the total metal dosage constant and, by extension, the total NP size. To control the relative radii of the cores and shells such that the NP plasmon tuning reflects the Ga:Mg ratio, we vary the relative dosages. The relative fraction of the core and shell metals is determined by the ratio of their fluxes in the gas phase according to ref 49 and taking into account the deposition rate of the two metals determined in our experimental conditions.

In situ spectroscopic ellipsometry[50] monitored in real-time the growth and the corresponding plasmonic response of the ensemble of nanoparticles by directly recording the pseudodielectric function $\langle\varepsilon\rangle = \langle\varepsilon_1\rangle + i\langle\varepsilon_2\rangle$, which is related to the NPs pseudoextinction coefficient $\langle k\rangle$ and refractive index $\langle n\rangle$ by the following equation:

$$\langle\varepsilon\rangle = \langle\varepsilon_1\rangle + i\langle\varepsilon_2\rangle = \sin^2\phi\left[1 + \tan^2\phi\,\frac{(1-\rho)^2}{(1+\rho)^2}\right] = \langle(n+ik)^2\rangle \quad (1)$$

where ϕ is the angle of incidence fixed at 70°

$$\rho = \frac{r_p}{r_s} = \tan\Psi e^{i\Delta} \quad (2)$$

is the ratio of the Fresnel reflection coefficients of the sample for the components of the polarized light parallel, r_p, and perpendicular, r_s, to the plane of incidence, measured through the ellipsometric angle Ψ is the amplitude ratio and Δ is the phase shift difference of the incident and reflected light beams.

Ellipsometric spectra were acquired every 1 s using a phase-modulated spectroscopic ellipsometer (UVISEL, Horiba Jobin Yvon) in the 0.75−6.5 eV spectral range with a 0.01 eV resolution.

The NPs chemical composition was also corroborated by X-ray photoelectron spectroscopy (XPS) using a monochromatic Al Kα source (Kratos Analytical Axis spectrometer). The Ga3d, O1s, and Mg2p, were acquired with pass energy of 17 eV. The binding energy scale was calibrated using the C1s photoelectron peak at 285 eV.

The nanoparticles were imaged by atomic force microscopy (AFM) performed in the intermittent-contact mode (IC-AFM) using an AutoProbe CP Thermomicroscope. A high aspect ratio probe-super sharp tip with a radius of curvature of 2 nm (ESP Series Probes-VEECO) was used.

The nanoparticles were also studied using high angle annular dark field (HAADF) imaging, conventional transmission electron microscopy (TEM), energy-filtered TEM (EFTEM) and electron energy loss spectroscopy (EELS), using a JEOL 2100 TEM equipped with a Gatan Image Filter and Tridiem digital camera. The EFTEM images were acquired for gallium $L_{2,3}$-edge and magnesium K-edge using the standard 3 window method and the optimum elemental mapping parameters calculated by use of a reference spectrum. Energy loss spectra were acquired in diffraction mode at 200 keV incident electron energy with collection semiangle three times greater than convergence semiangle.

Field emission scanning electron microscopy (FE-SEM) was also used to image the nanoparticles corroborating AFM data.

Discrete Dipole Approximation Calculations of Optical Properties. We have used the discrete dipole approximation (DDA), which is a numerical method used to calculate the electromagnetic interaction with targets of arbitrary shape, to calculate the optical properties of the core−shell nanoparticles.[51] According to the DDA approximation, the target, i.e., the nanoparticle, is discretized into a finite array of N polarizable cells, each of which has the same optical properties as that of the target location. The cells acquire dipole moments in response to the local electric field. For dielectric particles with permeability $\mu = 1$, the particle is solely represented by a collection of electric dipoles. Each electric dipole is characterized by a polarizability tensor $\bar{\bar{\alpha}}_j$ such that $\mathbf{P}_j = \bar{\bar{\alpha}}_j \mathbf{E}^{ext,j}$, where $\mathbf{P}_j$ is the instantaneous electric dipole moment and $\mathbf{E}_{ext,j}$ is the instantaneous electric field at position j due to all sources external to j, i.e., the incident radiation and the oscillating electric dipoles at all other $N - 1$ locations

$$E_{ext,j} = \bar{\bar{\alpha}}_j^{-1} P_j = E_{inc,j} - \sum_{k\neq j} A_{jk}^{(ee)} P_k \quad (3)$$

where $E_{inc,j} = E_0 \exp(ikr_j - i\omega t)$ is the electric field at position j due to the incident electromagnetic radiation and $-A_{jk}^{(ee)}P_k$ is the contribution to the electric field at position j due to the electric

dipole at position k:

$$A_{jk}^{(ee)}P_k = \frac{exp(ikr_j - i\omega t)}{{r_{jk}}^3}\left\{k^2 r_{jk}(r_{jk}P_k) + \left(1 - \frac{ikr_{jk}}{{r_{jk}}^2}\right)[{r_{jk}}^2 P_k - 3r_{jk}(r_{jk}P_k)]\right\} \quad (4)$$

The Clausius-Mosotti equation relates the microscopic electric polarizability for each electric dipole $\bar{\bar{\alpha}}_j$ and the local macroscopic electric permittivity $\bar{\bar{\varepsilon}}_j$ in the zero frequency limit $kd \rightarrow 0$, where k is the wavenumber of the incident radiation and d is the interdipole spacing. Incorporating the radiative correction in the polarizability[51]

$$\alpha_{eff,j} = \frac{\alpha_j}{1 - \left(\frac{2}{3}\right) i \left(\frac{\alpha_j}{d^3}\right)(kd)^3} \quad \text{with} \quad \alpha_j = \frac{3d^3}{4\pi}\frac{\varepsilon_j - 1}{\varepsilon_j + 2} \quad (5)$$

The DDA is a robust method that has been tested through comparisons with analytical methods,[52] especially with results calculated using the Lorenz-Mie theory,[53] which can be used to calculate the light scattered by a homogeneous sphere. Errors typically result from discretization of the sphere and can be reduced by increasing the resolution of the discretization by decreasing the cell size. Typical errors in the scattering intensities are on the order of 1%.

One of the benefits of the DDA is that calculations can be performed on any type of particle system, so long as it can be characterized within a discretized array. The only input parameters that are needed are the morphology of the system and the dielectric constants at each cell location. Such dielectric constants are routinely measured experimentally. For particle-substrate geometries, both the nanoparticle and the surface must be discretized, the latter of which is truncated to a value of thickness enough to reach convergence in a reasonable amount of time with a reasonable number of dipoles without sacrificing accuracy. Both parameters, i.e., the substrate thickness and the total number of dipoles, were changed and optimized in order to guarantee convergence in all cases analyzed.

It is important to emphasize that our analysis does not consider multiparticle interactions. In many situations similar to ours, samples are composed of a monolayer of particles in which multiple scattering occurs.[19,20] Generally, it has been shown that when multiple particles are placed upon a dielectric substrate of low refractive index (<2) like glass or sapphire, multiparticle scattering causes only slight changes in the plasmonic spectra, typically red- or blue-shifts of <0.3 eV. The final result is a broadening of the plasmonic spectrum that nevertheless retains the basic behavior of the isolated nanoparticle case.[54−56]

3. RESULTS AND DISCUSSION

Seeding the NP deposition with Ga establishes a fixed initial plasmon resonance to monitor during growth and we observe a distinct red-shift of the plasmon resonance upon initiating Mg deposition at a low flux (effective total dosage of 1.4 Å Mg), as shown by the real-time evolution of the extinction coefficient spectra for the NPs ensemble in Figure 1a. Assuming a room temperature sticking coefficient of 1 for both Ga and Mg, and beam flux ratios of 10:1 (Ga:Mg), Mg red-shifts the plasmon resonance at a faster rate than simply increasing the Ga dosage as a consequence of the smaller bulk plasma frequency of Mg and of

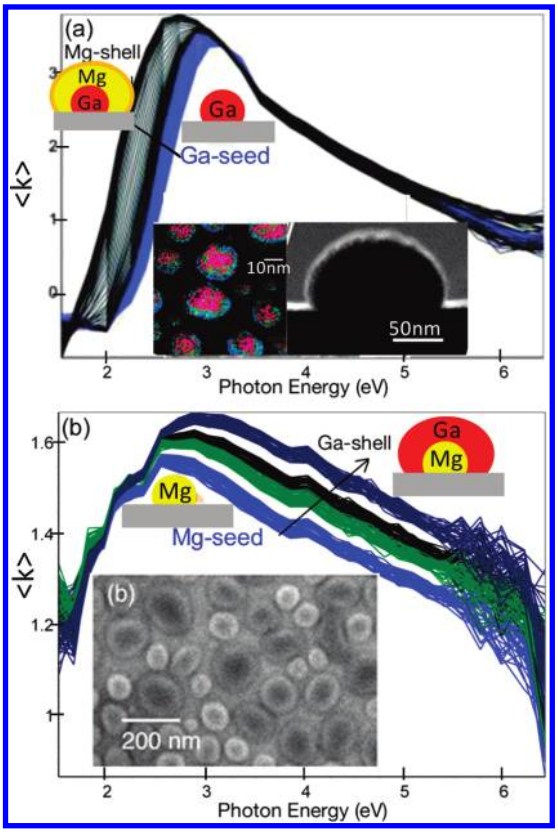

Figure 1. Real-time ellipsometric spectra of the extinction coefficient during deposition of (a) the Mg-shell (black) deposited onto Ga-core NPs (blue) and of (b) the Ga-shell deposited onto Mg core. Spectra are measured once per second and the Mg deposition clearly red-shifts the Ga NP SPR. The inset in (a) shows a HR-TEM image for the Mg-shell/Ga-core NPs supported on sapphire for larger NPs of approximately 100 nm diameter (light contour is for Mg map). A chemical element map (magenta-Ga, blue-Mg) is shown for smaller Ga-core/Mg-shell NPs. The inset in (b) shows a SEM electron backscattering micrograph for the Mg-core/Ga-shell NPs.

the increase of the shell thickness. From the electron energy loss spectra acquired during TEM analysis, plasmon energies of 13.8 and 10.3 eV have been experimentally measured for Ga and Mg, respectively (versus the theoretical 14.5 and 10.9 eV plasmon energies for Ga and Mg). Conversely, Figure 1b shows that when Mg seeds are created first and subsequently covered by a Ga-shell, the NP SPR blue-shifts, which is consistent with the higher Ga plasmon energy.

The core−shell structure of NPs can be seen in a typical HR-TEM image shown in the inset of Figure 1a for the Ga-core/Mg-shell case. A large NP shows a dark contrast hemispherical Ga core covered by light contrast Mg shell even for a short Mg deposition time. The inset in Figure 1a also shows the chemical element color map, Ga—magenta and Mg—blue, of smaller NPs. The chemical element map mainly shows that the Ga core is covered by a Mg shell, whose nonhomogeneity in color is due to its partial oxidation to MgO because of the air exposure of the samples and the tendency of Mg to oxidize as also supported by the XPS in the below.

The SEM electron backscattering micrograph is shown in the inset of Figure 1b for the Mg-core/Ga-shell case. The composition of the core−shell is further supported by the XPS data in Figure 2. The very narrow (FWHM = 0.9 eV) component at the

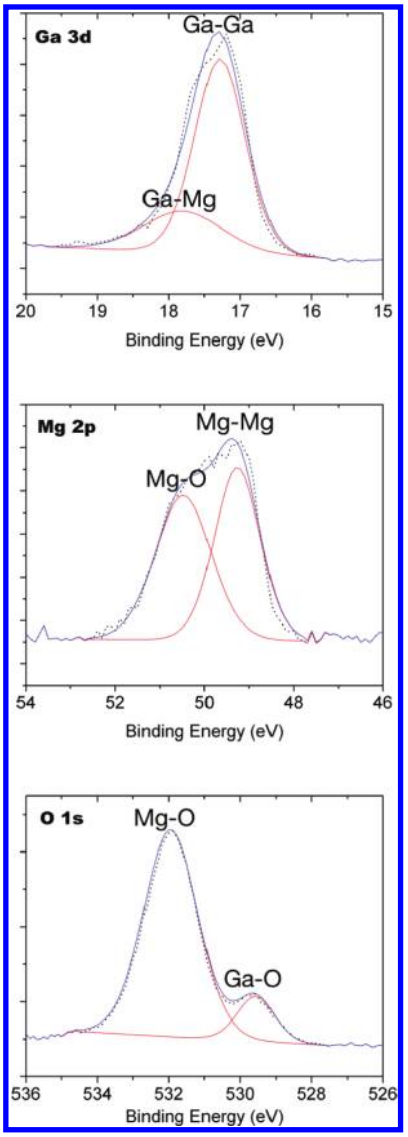

Figure 2. XPS spectra of the Ga3d, Mg2p, and O1s photoelectron core levels of the Ga-core/Mg-shell nanoparticles. Deconvolution of peaks into main fit components due to the metal and its oxide is also shown.

low binding energy (BE) of 17.5 eV in the Ga3d photoelectron peak can be attributed to the pure Ga metallic core, whereas the small tail at the higher binding energy side indicates slight intermixing at the Ga−Mg interface. Conversely, deconvolution of the Mg2p peak reveals two components attributable to the Mg shell (BE = 49.2 eV) and an outer shell of MgO (BE = 50.5 eV) due to NP air exposure. The O1s peak also supports the existence of the MgO outer shell (BE = 532.0 eV) surrounding the predominantly metallic Ga core (as confirmed by the negligible Ga-oxide component at 530 eV).

Previously, we have determined the Ga NPs exist in the liquid phase,[19] even at 25 °C, we therefore invoke the Mg solubility in Ga as factor compelling core−shell formation since the relative surface tensions of both metals, γ_{Ga} = 0.7 N/m and γ_{Mg} = 0.599 N/m drives the observed Mg segregation to minimize the NP surface energy.[57,58]

In order to deconvolute the effect of the NP overall size from the effect of the relative core-to-shell radii on the plasmon resonance, we fixed the total effective metal dosage, defined as

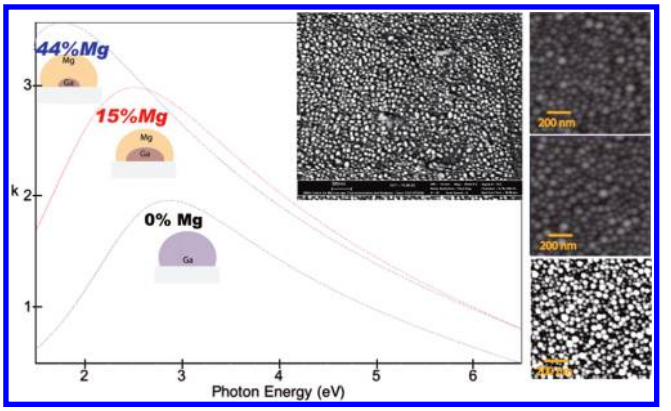

Figure 3. Extinction coefficient, *k*, spectra for Ga−Mg bimetallic NPs as a function of effective Mg percentage for a fixed total effective dosage of 12.4 nm (Ga + Mg) despite varying the relative composition. The corresponding AFM images are also shown, indicating a constant overall diameter of NPs. The FE-SEM image for the NPs with Mg volume percentage of 44% is also given in the inset to show that each nanoparticle is substrate supported and it is not a multilayer nanoparticle system.

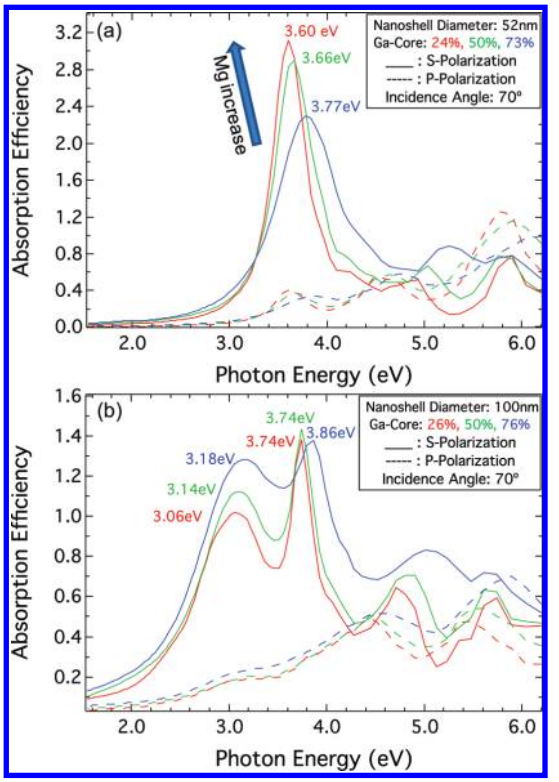

Figure 4. Absorption efficiency calculated by DDA for hemispherical Ga nanoparticles on a sapphire substrate with a diameter of (a) 50 nm and (b) 100 nm illuminated by s- or p-polarized beams, at an incidence angle of 70°.

the total effective thickness of metal deposited (nm). The core-to-shell size has been changed by the Mg/(Mg + Ga) flux ratio. Figure 3 shows the plasmon resonance red-shifts with increasing Mg volume percentage for NPs with a total diameter of 50−55 nm. This shifted single SPR absorbance band indicates coupling between the Ga and Mg layers and is consistent with a Ga core covered with a Mg shell.[59]

Figure 4 shows the DDA calculated absorption efficiency Q_{abs} as a function of photon energy for Ga-core/Mg-shell NPs of different overall sizes of (a) 52 nm and (b) 100 nm with increasing Mg volume percentage of shell. Q_{abs} has been chosen because it correlates directly with the measured imaginary part of the pseudodielectric function $\langle \varepsilon_2 \rangle$ (or $\langle k \rangle$), which is more tedious to calculate numerically and therefore not so accurate. The calculations are based on NPs supported on a finite sapphire substrate, and irradiated by a plane wave oriented at an angle of 70° with respect to the substrate normal, which matches the ellipsometric measurements angle. The plane wave is linearly polarized (similarly to the ellipsometric measurements). For linear s-polarized light, the electric field vector is perpendicular to the incident plane and is always parallel to the substrate. For linear p-polarized light, the electric field vector lies within the incident plane, so it has components both parallel and perpendicular. For the 52 nm NP case we used 34 000 dipoles. The size of the substrate was 150 nm × 150 nm. These values were 51500 dipoles and 300 nm × 300 nm respectively for the 100 nm NPs. A red-shift and an increase of the surface plasmon resonance are found for the 52 nm NPs with the increase of the Mg shell, consistently with data in Figures 3 and 1a.

A similar red-shift is observed with the increase of Mg shell also for larger NPs (see Figure 4b); however, in this case, more peaks can clearly be seen in the spectra, while for smaller NPs a SPR peak is more predominant. Indeed, it has also to be considered that part of the complexity of these spectra also comes from the nanoparticle−substrate interaction and the appearance of multipolar resonances as the NP size increases (in Figure 4b the narrow peak at 4 eV approximately to the right of the dipolar resonance (∼3 eV) corresponds to a quadrupolar resonance).

The experimental single peak for the smaller NPs (and also for the experimental data in Figure 3) can be explained considering that the major axis of the spheroids is in the range of 50 nm, which is smaller than the wavelength of the external electric field of radiation, i.e., we are in the quasi-static limit approximation, only a dipolar mode is observed, whereas for the larger NPs, i.e., >100 nm multipolar modes can be excited. Furthermore, according to the plasmon hybridization model,[60,61] we have to expect a lower energy mode, which corresponds to a symmetric coupling being dominated by the contribution from the plasmon resonance of the shell (Mg in the present case with a lower plasmon energy), and a higher energy antisymmetric mode with a dominant contribution from the core (Ga in the present case which has a higher plasmon energy).

The coupling and energies of these two resonances depend on the strength of the interaction between the shell and the core plasmons, which is controlled by the thickness of the shell layer. A thin shell results in strong plasmon mixing, which might also merge in one peak, while a thick shell yields separated plasmons of the two metals (the latter situation might be the case of the larger NPs).

Additionally, the lower amplitude of the asymmetric modes for the 50 nm nanoparticles (in Figure 4a), and the broad extinction coefficient spectra in Figures 1a and 3 due to the size distribution of the deposited NPs can also give a reason for the broad single experimental peak observed experimentally for the core−shell NPs.

We systematically tuned the Ga−Mg bimetallic NP plasmon using the effective Mg volume percentage and compared NPs with mean diameters of 100 and 50 nm, as shown in Figure 5. For comparison, Figure 5 (upper panel) shows that using pure Ga NPs to obtain the same variation of the plasmon resonance energy, the NPs size has to vary in the range 10−280 nm. By comparison, alloyed Au−Ag nanoparticles that range from pure Ag to pure Au whose plasmon resonance shifted less than 1 eV in total.

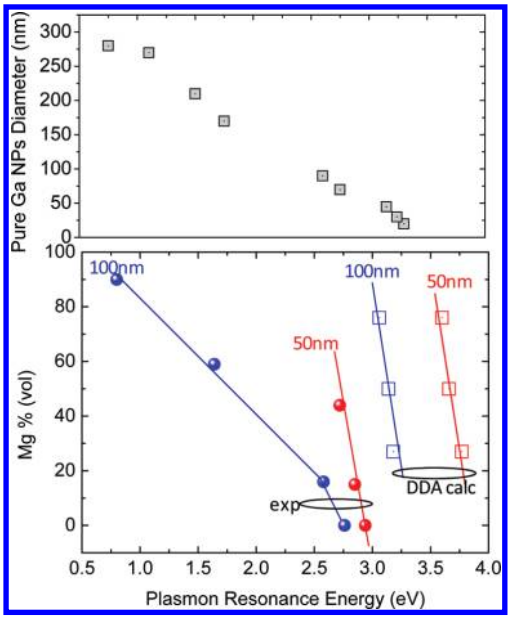

Figure 5. Variation of the SPR energy as a function of Mg volume percentage for the core shell nanoparticles of 50 and 100 nm diameters. Full symbols are for the experimental data from ellipsometry and empty square symbols are for calculated spectra from DDA. For comparison, the upper panel shows the diameter of pure Ga NP required to have the SPR varying in the same energy range.

It is interesting noticing that the slope of SPR energy variation with Mg percentage is independent of NP diameter (being the same for 50 and 100 nm NPs) according to DDA calculations and the same slope is found experimentally for the smaller 50 nm NPs. Conversely, 100 nm NPs show experimentally a different slope, i.e, the SPR energy variation per unit of Mg percentage is larger. This result can be explained by considering that the DDA calculations assumed hemispherical NPs, i.e., the aspect ratio of NPs is independent of size, leading always to the same slope, while for the experimentally deposited NPs, with the increase of size, become spheroids with the longer axis parallel to the substrate surface, and this change of the aspect ratio with the overall size increase give a reason of the change of the slope in Figure 5.

4. CONCLUSIONS

In summary, Ga−Mg core−shell NPs of controlled total size can be readily synthesized from the vapor phase using sequential deposition of the two constituent metals and initiated from Ga NP seeds. The resultant Ga−Mg NPs exhibit a plasmon resonance, tunable from the UV to the IR by tailoring the relative radii of the Ga core and the Mg shell, providing an additional degree of freedom in addition to NP size for modifying optical response. The Ga−Mg core−shell bimetallic system provides a valuable method by which plasmonic NPs can be red-shifted without increasing their total size. As an example, 100 nm Ga−Mg NPs can have a main resonance red-shifting from

approximately 3 to 0.5 eV by increasing the relative Mg % from 0 to 80%. The experimental observation of this red-shift monitored in real time by spectroscopic ellipsometry has been corroborated by discrete dipole approximation calculations. Indeed, the simulations provided for both small and large core−shell NPs clearly showed that multiple SPR peaks should characterize these bimetallic NPs. Certainly heterogeneity in the distribution of size of NPs, which also affect the interparticle interaction as well as the interaction of NPs with the substrate, is the main reason for broadening the plasmon resonance. Therefore, being proved the suitability of the Ga−Mg core−shell bimetallic NPs in yielding a SPR tunable from the near UV to the near IR, a further improvement in NPs homogeneity will certainly contribute to enhance the control and the applicability of the various plasmon resonance frequencies.

■ ACKNOWLEDGMENT

We acknowledge the support of ONR through the Grant N00014-08-1-0396. M.L. and G.B. acknowledge the European 7FP project "NanoCharM" (GA 218570). B.G.C. and F.M. thank Dr. F. González and Dr. P. Albella for their helpful comments. They also acknowledge project FIS2010-21984 from the Ministerio de Ciencia e Innovación of Spain.

■ REFERENCES

(1) Xia, Y.; Halas, N. J. *MRS Bull.* **2005**, *30*, 338348.
(2) Hutter, E.; Fendler, J. H. *Adv. Mater.* **2004**, *16*, 1685.
(3) Hen, H. M.; Liu, R. S. *J. Phys. Chem. C* **2011**, DOI: 10.1021/jp108403r.
(4) Wiley, B. J.; Chen, Y.; McLellan, J.; Xiong, Y.; Li, Z. Y.; Ginger, D.; Xia, Y. *Nano Lett.* **2007**, *7*, 1032.
(5) Carlos, E.; Román-Velázquez, C. E.; Noguez, C. *J. Chem. Phys.* **2011**, *134*, 044116 and reference therein.
(6) Bohren, C. F.; Huffman, D. R. *Absorption and Scattering of Light by Small Particles*; Wiley-VCH: Weinheim, Germany, 2004.
(7) Link, S.; El-Sayed, M. A. *J. Phys. Chem. B* **1999**, *103*, 4212.
(8) Henglein, A.; Giersig, M. *J. Phys. Chem. B* **1999**, *103*, 9533.
(9) McMahon, M.; Lopez, R.; Meyer, H.; Feldman, L.; Haglund, R. *Appl. Phys. B: Lasers Opt.* **2005**, *80*, 915.
(10) Kelly, K. L.; Coronado, E.; Zhao, L. L.; Schatz, G. C. *J. Phys. Chem. B* **2003**, *107*, 668.
(11) Mock, J. J.; Barbic, M.; Smith, D. R.; Schultz, D. A.; Schultz, S. *J. Chem. Phys.* **2002**, *116*, 6755.
(12) Link, S.; Mohamed, M. B.; El-Sayed, M. A. *J. Phys. Chem. B* **1999**, *103*, 3073.
(13) Jana, N. R.; Gearheart, L.; Murphy, C. J. *J. Phys. Chem. B* **2001**, *105*, 4065.
(14) Sun, Y.; Xia, Y. *Anal. Chem.* **2002**, *74*, 5297.
(15) Nehl, C. L.; Grady, N. K.; Goodrich, G. P.; Tam, F.; Halas, N. J.; Hafner, J. H. *Nano Lett.* **2004**, *4*, 2355.
(16) Balamurugan, B.; Maruyama, T. *Appl. Phys. Lett.* **2005**, *87*, 143105.
(17) Quinten, M. *Z. Phys. B Condensed Matter* **1996**, *101*, 211.
(18) Moresco, F.; Rocca, M.; Hildebrandt, T.; Henzler, M. *Phys. Rev. Lett.* **1999**, *83*, 2238.
(19) Wu, P. C.; Kim, T.-H.; Losurdo, M.; Bruno, G.; Everitt, H. O.; Brown, A. S. *Appl. Phys. Lett.* **2007**, *90*, 103119.
(20) Wu, P. C; Losurdo, M.; Kim, T. H.; Giangregorio, M.; Bruno, G.; Everitt, H. O.; Brown, A. S. *Langmuir* **2009**, *25*, 924.
(21) Maier, S. A.; Kik, P. G.; Atwater, H. A.; Meltzer, S.; HArel, E.; Koel, B. E.; Requicha, A. *Nat. Mater.* **2003**, *2*, 229.
(22) Atwater, H. A.; Maier, S.; Polman, A.; Dionne, J. A.; Sweatlock, L. *MRS Bull.* **2005**, *30*, 385389.
(23) Maier, S. A.; Atwater, H. *J. Appl. Phys.* **2005**, *98*, 011101.
(24) Sharma, A. K.; Mohr, G. J. *J. Phys. D: Appl. Phys.* **2008**, *41*, 055106.
(25) Habas, S. E.; Lee, H.; Radmilovic, V.; Somorjai, G. A.; Yang, P. *Nat. Mater.* **2007**, *6*, 692.
(26) Kalsin, A. M.; Pinchuk, A. O.; Smoukov, S. K.; Paszewski, M.; Schatz, G. C.; Grzybowski, B. A. *Nano Lett.* **2006**, *6*, 1896.
(27) Mulvaney, P. *Langmuir* **1996**, *12*, 788.
(28) Krasavin, A. V.; MacDonald, K. F.; Schwanecke, A. S.; Zheludev, N. I. *Appl. Phys. Lett.* **2006**, *89*, 031118.
(29) Raveendran, P.; Fu, J.; Wallen, S. L. *Green Chem.* **2006**, *8*, 34.
(30) Sablon, K. A. *Nanotechnology* **2008**, *19*, 125609.
(31) Stamenkovic, V. R.; Mun, B. S.; Arenz, M.; Mayrhofer, K. J. J.; Lucas, C. A.; Wang, G.; Ross, P. N.; Markovic, N. M. *Nat. Mater.* **2007**, *6*, 241.
(32) Torigoe, K.; Nakajima, Y.; Esumi, K. *J. Phys. Chem.* **1993**, *97*, 8304.
(33) Link, S.; Wang, Z. L.; El-Sayed, M. A. *J. Phys.Chem. B* **1999**, *103*, 3529.
(34) Lee, K. S.; El-Sayed, M. A. *J. Phys. Chem. B* **2006**, *110*, 19220.
(35) Wu, D.; Xu, X.; Liu, X. *Solid State Commun.* **2008**, *148*, 163.
(36) Zhu, J. *Nanoscale Res. Lett.* **2009**, *4*, 977.
(37) Motl, N. E.; Ewusi-Annan, E.; Sines, an T.; Jensen, L.; Schaak, R. E. *J. Phys. Chem. C* **2010**, *114*, 19263.
(38) Jana, D.; Dandapat, A.; De, G. *Phys. Chem. C* **2009**, *113*, 9101.
(39) Logsdail, A. J.; Cookson, N. J.; Horswell, S. L.; Wang, Z. W.; Li, Z. Y.; Johnston, R. L. *J. Phys. Chem. C* **2010**, *114*, 21247.
(40) Strawbridge, B.; Singh, R. K.; Beach, B.; Mahajan, S.; Newman, N. *J. Vac. Sci. Technol. A* **2006**, *24*, 1776.
(41) Yelon, A.; Piyakis, K. N.; Sacher, E. *Surf. Sci.* **2004**, *569*, 47.
(42) Krasavin, A. V.; Zheludev, N. I. *Appl. Phys. Lett.* **2004**, *84*, 1416.
(43) Wu, P. C.; Losurdo, M.; Kim, T.-H.; Choi, S.; Bruno, G.; Brown, A. S. *J. Vac. Sci. Technol. B* **2007**, *25*, 1019.
(44) Bennett, P. J.; Dhanjal, S.; Petropoulos, P.; Richardson, D. J.; Zheludev, N. I.; Emelyanov, V. I. *Appl. Phys. Lett.* **1998**, *73*, 1787.
(45) Wu, P. C.; Kim, T. H., Suvorova, A.; Giangregorio M. M.; Saunders, M.; Bruno, G.; Brown, A. S.; Losurdo, M. *Small*, **2011**, DOI: 10.1002/smll.201002064.
(46) Yao, X.; Wu, C.; Du, A.; Lu, G. Q.; Cheng, H.; Smith, S. C.; Zou, J.; He, Y. *J. Phys. Chem. B* **2006**, *110*, 11697.
(47) Collins, S. E.; Baltanás, M. A.; Bonivardi, A. L. *Langmuir* **2005**, *21*, 962.
(48) Draine, B. T.; Flatau, P. J. *J. Opt. Soc. Am. A* **2008**, *25*, 2693.
(49) Wood, C. E. C.; D. Desimone, D.; Singer, K.; Wicks, G. W. *J. Appl. Phys.* **1982**, *53*, 4230.
(50) Losurdo, M.; Bergmair, M.; Bruno, G.; Cattelan, D.; Cobet, C.; de Martino, A.; Fleischer, K.; Dohcevic-Mitrovic, Z.; Esser, N.; Galliet, M.; Gajic, R.; Hemzal, D.; Hingerl, K.; Humlicek, J.; Ossikovski, R.; Popovic, Z. V.; Saxl, O. *J. Nanopart. Res.* **2009**, *11*, 1521.
(51) Collinge, M. J.; Draine, B. T. *J. Opt. Soc. Am. A* **2004**, *21*, 2023.
(52) Lévêque, G.; Martin, O. J. F. *Opt. Express* **2006**, *14*, 9971.
(53) Noguez, C. *Opt. Mater.* **2005**, *27*, 1204.
(54) Su, K.-H.; Wei, Q.-H.; Zhang, X.; Mock, J. J.; Smith, D. R.; Schultz, S. *Nano Lett.* **2003**, *3*, 1087.
(55) Rechberger, W.; Hohenau, A.; Leitner, A.; Krenn, J. R.; Lamprecht, B.; Aussenegg, F. R. *Opt. Commun.* **2003**, *220*, 137.
(56) Kottmann, J. P.; Martin, O. J. F. *Opt. Lett.* **2001**, *26*, 1096.
(57) Weast, R. C.; Lide, D. R.; Astle, M. J.; Beyer, W. H. *CRC Handbook of Chemistry and Physics*; CRC Press Inc.: Boca Raton, FL, 1989.
(58) Hashim, J.; Looney, L.; Hashmi, M. S. J. *J. Mater. Processing Technol.* **2001**, *119*, 324.
(59) Shore, M. S.; Wang, J.; Johnston-Peck, A. C.; Oldenburg, A. L.; Tracy, J. B. *Small* **2011**, *7*, 230.
(60) Prodan, E.; Nordlander, P. *J. Chem. Phys.* **2004**, *120*, 5444.
(61) Prodan, E.; Radloff, C.; Halas, N. J.; Nordlander, P. *Science* **2003**, *302*, 419.